American Journal of Engineering Research (AJER)
e-ISSN: 2320-0847 p-ISSN : 2320-0936
Volume-13, Issue-12, pp-124-135
www.ajer.org
Research Paper Open Access

Numerical Modelling of Compressive SHPB Testing for Predicting Dynamic Impact Response of AA 2519-T8 Aluminum Alloy

[1*]Abu R. and [1]Patani W.
[1]*Department of Mechanical Engineering, University of Ibadan, Ibadan, Nigeria*
Corresponding Author: aburahaman@yahoo.com

ABSTRACT: *Aluminium alloys, particularly AA 2519-T8, are critical in high-risk applications such as aerospace and defense due to their high strength-to-weight ratio, corrosion resistance, and formability. This study addressed the limitations of experimental high-rate-loading methods, specifically the Split Hopkinson Pressure Bar (SHPB) technique, by developing a computational model to simulate the dynamic behaviour of AA 2519-T8 under impact loading. Utilizing finite element analysis with Neper and Abaqus software, the study modelled the SHPB setup and predicted the mechanical response of the alloy at various strain rates. Results from the computational model were compared with experimental data from the literature to validate the model's accuracy, showing a promising correlation with less than 5% error in peak stresses across different strain rates. This work demonstrated the viability of computational methods as a cost-effective and accessible alternative to traditional experimental approaches in high strain-rate material testing.*
KEYWORDS: *Aluminium alloy, Split-Hopkinson Pressure Bar, Dynamic impact loading, High strain-rate testing, Finite element analysis*

Date of Submission: 12-12-2024 Date of acceptance: 25-12-2024

I. INTRODUCTION

Aluminium alloys are widely used in the industry due to their high strength-to-weight ratio, good corrosion resistance, and excellent formability. The Aluminium Association (AA), AA 2000 series, is one of the many types of aluminium alloys that is frequently used in aerospace, automotive, construction, and defense applications [1]. The AA 2519-T8 aluminium alloy, which is an armor grade alloy with copper and manganese serving as the primary alloying components is one of the many class of the AA 2000 family that finds its use in defense application. The "T8" designation represents the heat treatment condition; indicating that the alloy has been artificially aged to reach the appropriate strength and hardness [2].

Owing to its high-risk applications, prevention and mitigation of these unpleasant scenarios necessitates a need to investigate how various engineering materials perform under the different conditions imposed during actual applications. The vital information needed to create predictive constitutive model description of materials are supplied by high-rate-loading experimental studies.

Over the years, several methods such as Taylor Impact [3], Dynamic Indentation [4] and Split Hopkinson pressure bar methods are generally used for characterizations of material properties. Out of these methods, the Split Hopkinson Pressure Bar (SHPB) experimental setup has become popular for determining the dynamic behaviour of material at high strain rates. However, constraints such as cost, well-trained laboratory personnel, high precision requirements, complicated material preparation and data acquisition/processing etc., make this tool typically expensive and not viable for use by the majority of engineers that desire it for most practical applications. Hence, this all important tool has been limited to Ivy League institutions and high-tech companies who can afford the cost and provide the needed manpower. It is therefore imperative that alternative methods be found to derive the necessary performance statistics in a cost and time efficient manner that gives values which closely mirror those derived by experimental and mathematical means for real-life application of engineering materials. These values will enable manufacturers, fabricators and engineers to determine if a

material successfully meets design specifications and standards in a design problem.

This study aims at bridging the gap as much as possible by creating a computation model of the compressive SHPB testing set-up and using this model to generate the mechanical response of the aluminium-copper alloy AA2519-T8 to dynamic impact loading. AA2519-T8 is a material commonly employed in engineering systems and processes which require and/or benefit from high strain-rate material testing.

Many researchers have attempted using computational methods as a supplementary tool to study the behaviour of materials during various dynamic loading conditions. For instance, Xie et al. [5] used numerical models and the SHPB experimental data to examine how various coal and rock combinations behaved while the striker's velocity ranged from 4.590 to 8.791 m/s. Sulaiman et al. [6] (2019) used SHPB to investigate the impact strength of refined grain pure copper at high strain rates both computationally and experimentally. The yield strength and ultimate strength were observed to increase by 68% and 128%, respectively, at strain rates of 1200 s−1. The numerical results agreed with the experimental findings published by Olasumboye et al. [7].

Other researchers also considered using computational models to study the SHPB experimental setup in other to find grounds to improve the system. For instance, Zhang et al. [8] used ANSYS/LS-DYNA software to run finite element simulations of split Hopkinson pressure bars to understand the dynamic compressive behavior of hat-shaped specimens of AZ31B magnesium alloy. It was shown that when the strain rate rose, the impacts of thermal softening were reduced. Afdhal et al. [9] used simulation to investigate the effects of specimen shape and bar straightness on SHPB measurement and discovered that the specimen shape had the most influence on the outcomes. To comprehend the significance of shape. Gupta [10] examined the finite element behavior of AA7075 under the square shape of the striker of SHPB with varied loads. Under dynamic situations, the shape of the specimen and striker bar varies from square to circular.

Although these techniques are found useful in studying the SHPB configuration and are often used in conjunction with the SHPB experimental setup, they do serve as a validated alternative that can be used for predictive purposes in situations where the experimental setup is not visible.

The growth of the theory of finite element analysis and the increasing need for a variety of engineering simulation programs, such as ANSYS, ABAQUS and others that are built on the principles of FEA, has made the modelling of experimental setups and predicting the behaviour of the material under various real-world application scenarios possible in engineering practice [11-13]. However, it is necessary to verify the appropriate modelling setup for various applications by comparing the results with proven results obtained from the exact experimental setups available in the literature. Verified model settings for determining the AA 2519-T8 alloy that can function as a trustworthy stand-in for actual configurations were not readily available at the time this study was conducted.

II. METHODOLOGY

To undertake numerical investigations of the microstructural evolution of materials, the geometrical attributes of the grains must be modeled. However, the experimental procedure that assists this process is cumbersome. To reduce this complexity, the Voronoi tessellation is a widely used approximation method for the microstructure of polycrystalline materials. Various computer programs built on this tessellation, such as Neper and Dream 3D, are often used to approximate the real microstructure for any number of grains. Neper which includes a module for meshing the created structure, it was utilized in this study to generate the tessellation. The output was then imported into Abaqus as .inp file for further analysis.

A cylindrical test specimen is used in this simulation. Using a cylindrical test specimen is valid as experimental test results for a similar specimen reported by Olasumboye et al. [7]. The specimen length/diameter is fixed at 3.3 mm/Ø3.3 mm. Hence the simulation was done with an aspect ratio of L/D=1 as shown in Fig. 1.

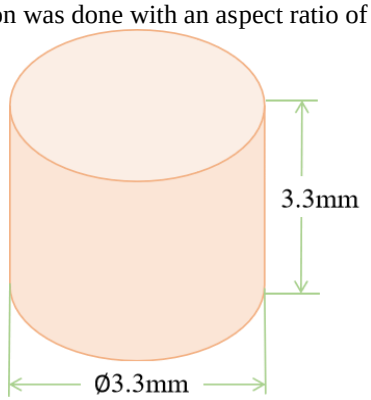

Fig. 1. Cylindrical shaped test specimen

The pressure bars was designed with an L/D ratio of 146.54, which conforms to the dimensions stated in the literature. A diameter of 13 mm was assumed for the pressure bars which was based on Olasumboye et al. [7]. The diameter of the striker bar was fixed by that of the pressure bars to be 13 mm while a striker bar length of 700 mm was used for the simulation.

2.1. AA2519-T8 Material Properties

Olasumboye et al. [7] and Macar [14] were used to compile the properties of AA2519-T8. In order to correctly model the test specimen response to dynamic impact loading at the different specified strain rates, the test specimen material was better modelled as elastoplastic. The elastic mechanical properties of AA2519-T8 used for material definition in Abaqus are given in Table 1.

Table 1. Properties of AA2519-T8 used in model

Mechanical Properties:		
Density:	Young's Modulus:	Poisson's Ratio:
2813.36 kg/m^3	74.466 GPa	0.33
Thermal Properties:		
Specific Heat Capacity:	Thermal Conductivity:	Inelastic heat fraction:
980 J/kg.°C	160 W/m.°C	0.9

Knowing that the specimen is expected to be deformed into the plastic zone during the impact, Abaqus requires plastic property data and a description of the plastic behaviour of the material. Unfortunately, the plastic behaviour of materials for dynamic loading conditions varies and can only be obtained through rigorous experimental methods such as the SHPB which is an area this study intends to avoid. However, the static plastic properties of the material were reported to be more stable [14, 15]. Hence, the static plastic properties were employed as the inputs to forecast the dynamic response of the material.

2.2. Ti–6Al–4V Material Properties

One of the fundamental test criteria for compressive SHPB testing is that no pressure bar employed in the test setup may have its elastic limit exceeded. As a result, the material of the pressure bar is modeled as simple elastic. Additionally, it had been reported that the incident bar, sticker bar, and transmitted bar need to be composed of the same material by Olasumboye et al. [7]. Therefore, the pressure bars were modelled with titanium aluminum vanadium (Ti–6Al–4V) alloy with a density of 4430 kg/m^3, Young's Modulus of 114 GPa and Poisson's ratio of 0.342.

2.3. SIMULATION: MODELLING AND ANALYSIS

The synthetic microstructure was generated using NEPER. The generated synthetic microstructure is imported into ABAQUS as synthetic microstructure model in an '.inp' file format for further processing. Abaqus/CAE was divided into modules, where each module defined a logical aspect of the modelling process. The modules were arranged in an order that was realistically followed in creating a simulation from the modelling to the analysis and results visualization. However, there was freedom to switch between the different modules as required by the user during a simulation. The modules were arranged as shown in Fig. 2.

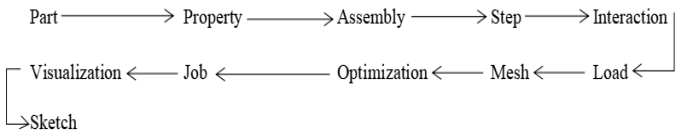

Fig. 2. Abaqus modelling workflow

The above order of the modules was loosely followed in creating the necessary simulations. Six simulations were carried out on a Ø3.3 mm x 3.3 mm cylindrical-shaped test specimens at 1000, 1500, 2000, 2500, 2500 and 3500 s^{-1} strain rates, including adiabatic effects

The components of the SHPB model like the pressure bars and striker bars with the appropriated dimensions were created as 3D, deformable solid extrusion and shaped solid by using the part module on Abaqus/CAE. All created parts are brought together by instancing the parts and positioned as in an actual experiment using position constraints using the assembly module. Furthermore, features, sets and surfaces were created which allowed for easy application of initial and boundary conditions.

The created parts were assigned the appropriate mechanical and thermal properties of the material which determined their responses in the analysis. The pertinent properties in this study are:
(i) Mechanical Properties: Density, Young's modulus, Poisson's ratio to define its elastic properties and the yield stress (true stress), and plastic strain (true plastic strain) that determines the plastic properties.
(ii) Thermal Properties: Conductivity, specific heat capacity and inelastic heat fraction.

For the computational model, it was assumed that friction did not exist between the bars and the test specimen. A hard, frictionless interaction property was defined between the striker bar, incident bar, test specimen and transmitted bar. Consequently, There was explicit surface-to-surface contact between the striker bar and the incident bar, the incident bar and the test specimen, the test specimen and the transmitted bar and an explicit general contact for all instances in the assembly (Fig. 3).

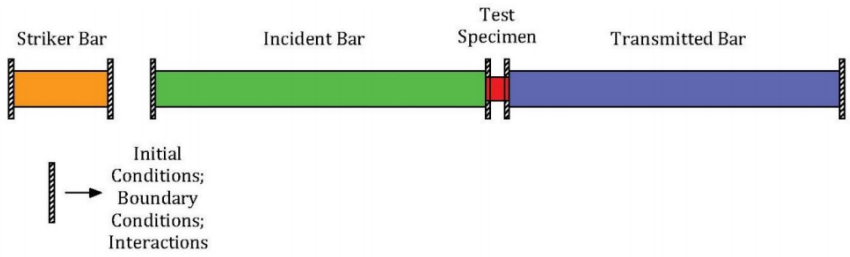

Fig. 3. Schematic diagram of the computational SHPB model

The penalty contact method with finite sliding was used with the frictionless interaction property. As in an actual test, it was expected that the test specimen would fly off from its pre-simulation position as the simulation progressed. The explicit general contact was crested as a precaution against interpenetration of assembly instances during the simulation.

Boundary conditions (BCs) were also applied to those regions of the model where the displacements and/or rotations were known. Such regions may be constrained to remain fixed (have zero displacement and/or rotation) during the simulation or may have specified, non-zero displacements and/or rotations. Four BCs which included displacement/rotation BC on the striker bar, displacement/rotation BC on the incident bar, displacement/rotation BC on the transmitted bar, and symmetry/antisymmetry/encastre BC on the free end of the transmitted bar were applied to the model.

The displacement/rotation BCs constrained the bars to translate only in the z-direction (U3) while rotations in all directions (x, y and z) were allowed. This ensured precise bar alignment to aid both uniform and one-dimensional wave propagation within the pressure bars as well as for uniaxial compression within the test specimen during loading which is also the case in the real time experiment [16]. The symmetry/antisymmetry/encastre BC constrained the translation of the free end of the transmitted bar in all directions (x, y and z) to zero while rotations in all directions (x, y and z) were allowed. This BC replaced the momentum trap or absorber which stops the movement of the transmitted bar at the end of an experiment.

After creating the BCs, the analysis steps are configured. In this computational model, the dynamic response of the incident bar, test specimen and transmitted bar was being studied as a single event, so only a single analysis step was required for the simulation. However, an initial step, in which boundary conditions that constrained the movement of the various components was applied and an Abaqus/Explicit step with a step time of 0.0125 s, was created, in which an initial velocity condition was applied to the striker bar.

Abaqus/Explicit is a specialized analytical tool that employs an explicit dynamic finite element formulation. It is very effective for highly nonlinear issues requiring changing contact conditions, like forming simulations, and is appropriate for modelling brief, transient dynamic events, including impact and blast problems [17].

Initial conditions or constraints were also applied to assembly instances which take effect right at the beginning of the simulation, Initial conditions in Abaqus were termed 'predefined fields' and included parameters such as velocity, temperature, geostatic stress, pore pressure.

The strain rate induced in the aluminium-copper alloy AA2519-test specimen ($\dot{\varepsilon}$) is mainly determined by the velocity of the striker bar (V_{st}) and the length of the test specimen (L_s). Equation (1) is used to obtain the velocity to be applied to the striker bar with a correction factor of 1.25.

$$V_{st} = \dot{\varepsilon} L_S * 1.25 \quad (1)$$

For the current computational model, a velocity-predefined field was applied to the striker bar at the initial step. This replaced the components required to launch the striker bar in an actual SHPB set-up such as the

gas cylinder, launching barrel, pressure regulators and pressure valves. The default settings were ideal for generating mesh and were used for this study.

Having completed every necessary step in the simulation process, the outputs were generated. Abaqus simulations can produce a considerable amount of output. Thus only the output necessary for analyzing the results was made available to prevent using up too much disk space. The analysis's results were automatically written by Abaqus/ to an output database (*.odb) file. Field output and history output are requested. The stress component and invariant (S33), Logarithmic strain component (LE33), Plastic strain component (PE33), Mechanical strain rate component (ER33), Element Temperature (TEMP) rate and temperature data were requested as history outputs. Similar data was also requested as field output to reduce disk space and computational time.

Finally, a job was created. The job creation process commanded Abaqus/CAE to convert the parts, assembly, loads, interactions and mesh into an input file which was read by Abaqus/Explicit and solved using the appropriate equations with output requests written to the .odb file for post-processing. After the job, the visualization module could be accessed to view contour plots of the deformed shape as a graphic view of the analysis results. XY data was created from the .odb history output to give graphs that plot the requested output variables against time. The XY data could be further operated upon by combining, truncating, and smoothing.

III. RESULTS AND DISCUSSION

The basic underlying principles of the compressive SHPB were implemented in the development of a computational model of the actual experimental set-up. All the components of the actual set-up were modelled using parts, assemblies, initial and boundary conditions, interaction properties and interactions to give the computational SHPB model. The output of the simulation was hereby presented for discussion.

3.1. STRIKER BAR VELOCITIES

After numerous simulations and analyses, this study presented the results of six simulations carried out on an aluminium-copper alloy AA2519-T8 test specimen.

The plot of the strain rate versus (vs) striker bar velocity that was used in the model is also shown in Fig. 4. A Co-efficient of Determination (R^2) of 0.9948 shows that the strain rate was approximately a linear function of the velocity of the striker bar.

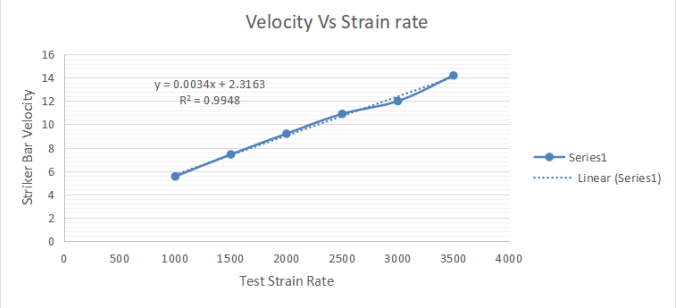

Fig. 4. Striker bar velocity vs test strain rate

The output data obtained from the computational model were compared with the experimental data from olasumboye et al. [7]. The results of simulations in the computational study were presented in subsequent sections based on the strain rates of the test specimen.

3.2. TEST SPECIMEN RESULTS

The first output to be obtained was the strain rate impacted on the specimen. This was important because the true stress and strain were expected to be recorded at specific strain rates. A valid strain rate vs time plot should register a zero strain rate before the impact. After the impact, the strain rate rose suddenly to a peak value and then fluctuated around lesser values before returning to zero within a short period. This described a typical impact and repulsion between the striker bar and the incident bar which mimicked the actual situation. A typical strain rate vs time curve is shown in Fig. 5.

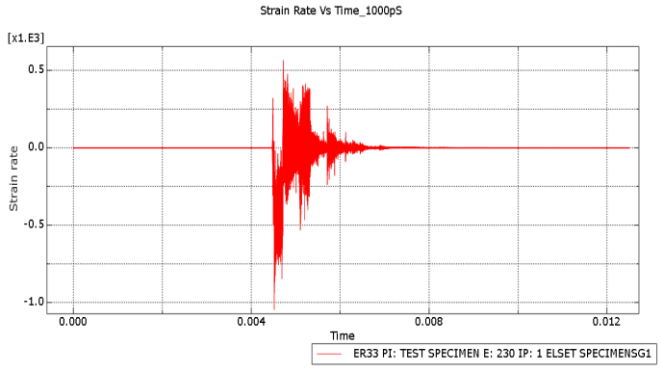

Fig. 5. Strain rate (s^{-1}) vs time curve for test specimen at 1000 s^{-1}

At a striker bar velocity of 5.53, 7.42, 9.2, 10.9, 12.0 and 4.2 m/s the computational model recorded a strain rate of 1047.48, 1485.5, 2051.4, 2563.3, 3025.3, 3537.4 s^{-1} which gave approximate strain rates of 1000, 1500, 2000, 2500, 3000, 3500s^{-1}, respectively. Having verified the strain rates, the true stress vs true strain plots were also generated and found to compare reasonably with the experimental data extracted from olasumboye et al. [7] as shown in Fig. 6 and Fig. 7.

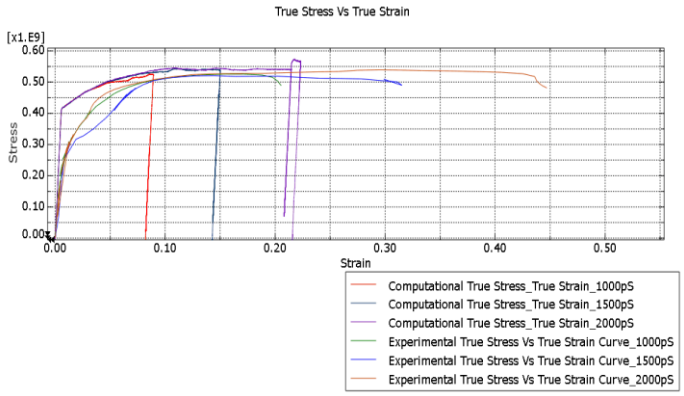

Fig. 6. Computational and experimental true stress vs true strain at 1000, 1500, 2000s^{-1}

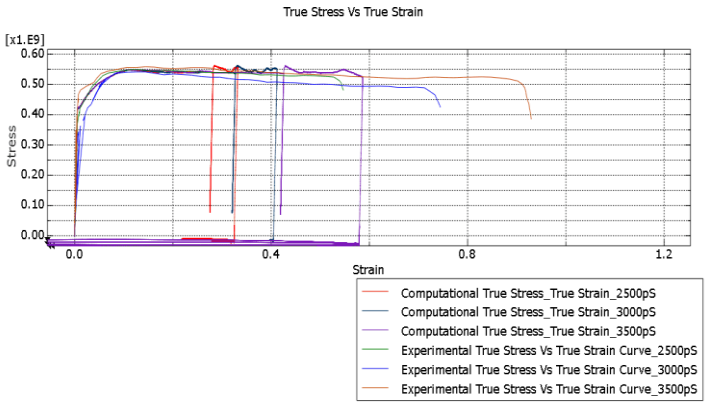

Fig. 7. Computational and experimental true stress vs true strain at 2500, 3000, 3500s^{-1}

The summary of the result is presented in Table 2.

Table 2. Summary of experimental and computational results for ∅3.3 mm x 3.3 mm AA2519-T8 test specimen

Strain Rate		Peak True Stress (MPa)			Max True Strain			Temp-C. (ΔT) (°C)
Emp.	Comp.	Exp.	Comp.	Error	Exp.	Comp.	Error	Comp
1000	1047.48	528	526	0.3788%	0.2	0.082	59.00%	13.25
1500	1485.5	523	540	-3.25%	0.3	0.14275	52.42%	24.1
2000	2051.4	542	565	-4.244%	0.4	0.2154	46.15%	37.15
2500	2563.34	552	568	-2.899%	0.55	0.325	40.91%	56.58
3000	3025.3	545	560	-2.752%	0.7	0.404	42.28%	70.73
3500	3537.4	560	560	0.00%	0.9	0.5795	35.6%	101.17

Emp. =Empirical, Exp. = Experimental, Comp. = Computational, Temp-C. = Temperature Change

3.3. Strain rate

For this computational model, all strain rates were verified and considered valid, allowing further post-processing. However, it was observed that with the increase in strain rate, there was a progressive decrease in the rate at which the vibration induced by the transmitted stress wave died out. This may be due to the increased vibration frequency due to the increase in velocity of the striker bar. Fig. 8 shows a plot of the stress vs time at a strain rate of $1000s^{-1}$ and $3500s^{-1}$ to further buttress this point.

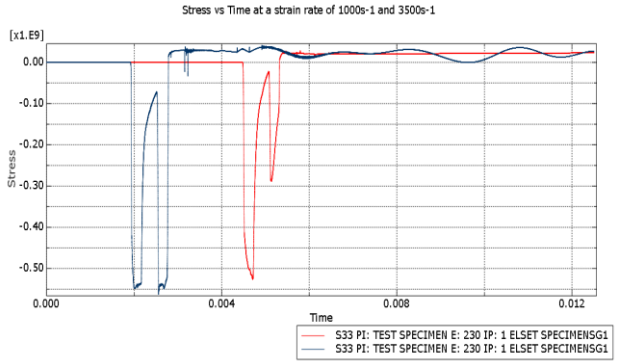

Fig. 8. Stress vs time at a strain rate of $1000s^{-1}$ and $3500s^{-1}$

3.4. Stress – Strain Curves

The true stress–true strain curves for the AA2519-T8 aluminium alloy obtained at six different strain rates obtained from computational model are presented in Fig. 6 and 7.

Since strain rate dependent plastic properties are not readily available in the literature, the static properties are used in the computational model. This sets in some slight discrepancies owing to the fact that in Abaqus, the plastic properties inputted into the model are retained as the material is deformed into the plastic regime. The implication of this is that all the stress-strain curves appears to follow a predefined path and the yield point is obviously fixed at an average of 420 MPa in the model for all strain rates. This result was justified because even though it is reported in Olasumboye et al. [7] that the yield point is sensitive to strain rate, it was also confirmed that the yield point at lower strain rates appeared to be unclear and that the yield point of all strain rates especially at higher strain rates averaged around the yield point of the quasi static loading condition. Thus, the yield point of the quasi static loading condition could be accepted as a good approximation for modelling purposes because with increase in strain rate, the yield point tends to get closer to that obtained from

Olasumboye et al. [7].

Peak stresses: Just like the peak stresses reported in Olasumboye et al. [7], the peak stresses from the computational model also experienced a variation that showed strain rate sensitivity. Peak flow stresses of 526, 540, 565, 568, 560 and 560 MPa were observed at strain rates of 1000, 1500, 2000, 2500, 3000 and 3500 s^{-1}, respectively. These values constituted 99.62, 103.25, 104.2, 102.9, 102.75 and 100% of the experimental findings reported in Olasumboye et al. [7] with an error of 0.3788, -3.25, -4.244, -2.899, -2.752 and 0.00% at strain rates of 1000, 1500, 2000, 2500, 3000 and 3500 s^{-1} respectively. These results are within acceptable limits as they maintain a maximum error that is below 5% for all strain rates.

Plastic flow: Another important result from the true stress-strain curves obtained from the computational model was the extent of deformation experienced by the material at various strain rates. An initial strain hardening was observed followed by an approximately perfect plastic flow which increased with an increase in strain rate. A true strain of 0.082, 0.14275, 0.2154, 0.325, 0.404 and 0.5795 were recorded at strain rates of 1000, 1500, 2000, 2500, 3000 and 3500 s^{-1}, respectively. These values constituted 41.26, 47.58, 53.85, 61.32, 57.7 and 64.38%, respectively of the experimental findings reported in Olasumboye et al. [7] with errors of 59.00, 52.42, 46.15, 40.91, 42.28 and 35.6% at strain rates of 1000, 1500, 2000, 2500, 3000 and 3500 s^{-1} respectively. While these results may not find justification in themselves, it could easily be observed that the errors of the results were within a close range with a general trend of the model accuracy increasing with strain rate. Hence, with an appropriate correction factor as a function of strain rate and material property, the results will yield very valid results. In an attempt to illustrate this point, plots were done by scaling the true strains of the computational models and were compared with experimental results reported in Olasumboye et al. [7] as shown in Fig. 9 through Fig. 14. The results obtained by scaling the true strains for the strain rates of 1000, 1500 and 2000s^{-1} by a factor of 2.3, 2.2 and 2.2, respectively and the strain rates of 2500, 3000 and 3500 s^{-1} by a factor of 1.7, 1.8 and 1.9, respectively yielded results that were within acceptable limits. Hence using an average of 2.2 for lower strain rate between 500 to 2499 s^{-1} and an average of 1.8 for higher strain rates above 2500 would be a justified correction factor. Alternatively, using a general correction factor of 2.0 would yield considerable results as well. Additionally, the variations in the true stress vs. true strain curve obtained from the computational model were similar to those reported by Olasumboye et al. [7] across a range of low to high strain rates. This is a huge breakthrough in the computational modelling of the material using the SHPB setup.

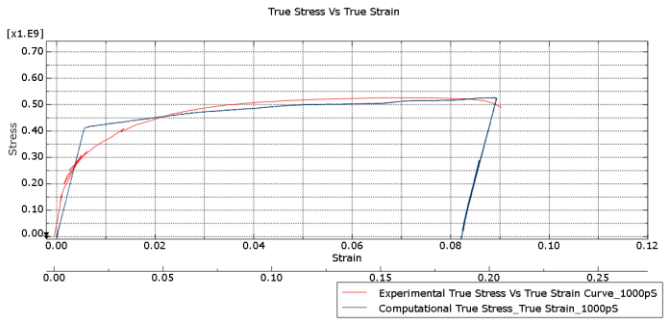

Fig. 9. Computational strain scaled by 1:2.3 and experimental strain at 1000s^{-1}

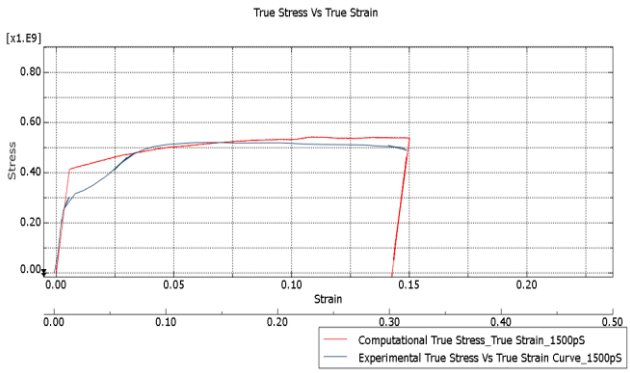

Fig. 10. Computational strain scaled by 1:2.2 and experimental strain at 1500 s^{-1}

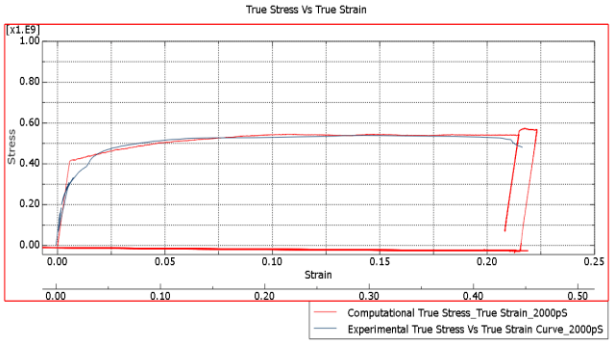

Fig. 11. Computational strain scaled by 1:2.2 and experimental strain at 2000 s^{-1}

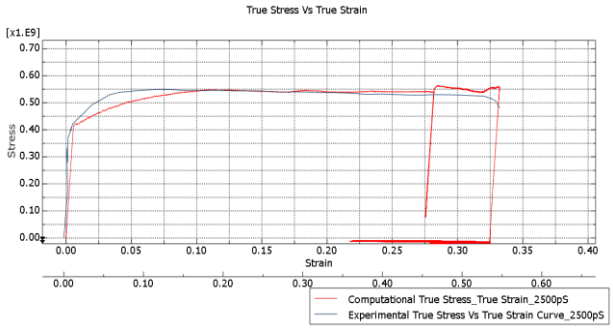

Fig. 12. Computational strain scaled by 1:1.7 and experimental strain at 2500 s^{-1}

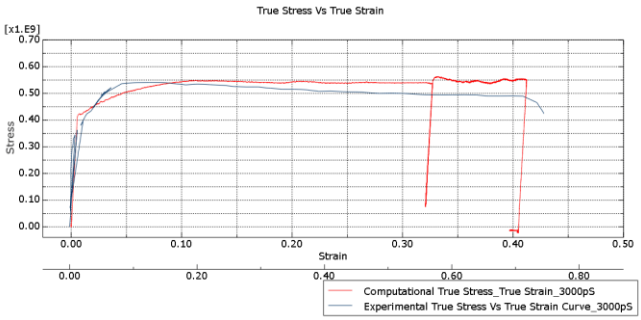

Fig. 13. Computational strain scaled by 1:1.8 and experimental strain at 3000 s^{-1}

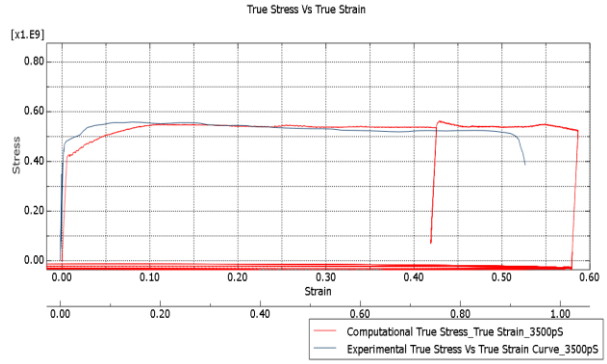

Fig. 14. Computational strain scaled by 1:1.9 and experimental strain at 3500 s^{-1}

3.5. Temperature Changes

It was also noticed that at lower strain rates such as 1000, 1500 and 2000 s^{-1}, there was a negligible distortion in the plastic flow whereas at higher strain rates such as 2500, 3000 and 3500 s^{-1} a noticeable distortion evolved. This suggested deformation information that could not be properly captured. As reported in by Owolabi et al. [18], this could be the result of thermomechanical instabilities, which were behaviours caused by thermal softening. Temperature variations upon impact were also requested as part of the simulation's output to verify this claim. With strain rates of 1000, 1500, 2000, 2500, 3000, and 3500 s−1, a maximum temperature change of 13.25, 24.1, 37.15, 56.58, 70.73, and 101.17ºC were noted, respectively.
A plot of Temperature against Strain rate in Fig. 15 showed that there was a higher increase in temperature from strain rates of 2500 s^{-1} and above when compared with that of lower strain rates. This indicated the possibility of increased thermal instabilities which was evident in the increased distortion in plastic deformation at strain rates of 2500 s^{-1} and above as shown in the respective true stress vs true strain curves (Fig. 15).

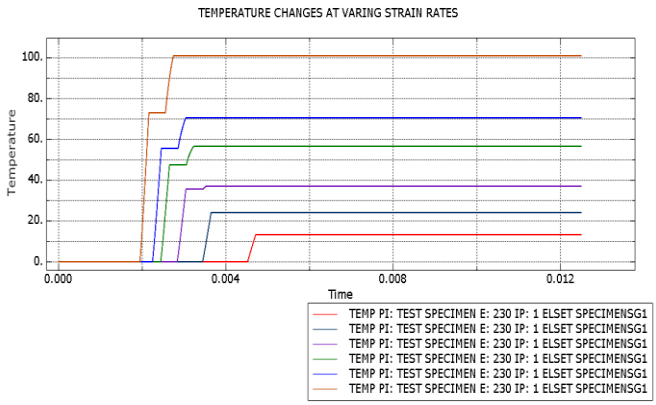

Fig. 15. Temperature changes at varying strain rates against time

3.6. Microstructure Evolution

A contour plot of the equivalent plastic strains (PEEQ) for all strain rates reveals that the deformation was heterogeneous which also corresponds to what was reported in Olasumboye et al. [7]. Fig. 16 shows the optical micrograph of a specimen deformed at 3500 s^{-1} obtained in the experiment, compared reasonably against the PEEQ, generated in the computational model at the same strain rate.

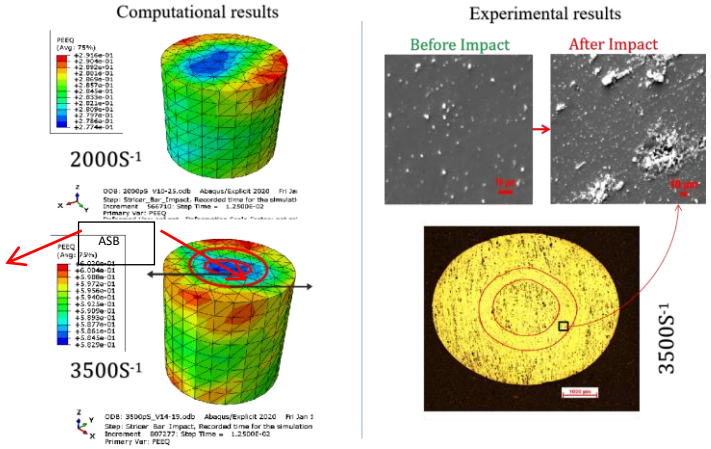

(a) Computation model (b) Experiment

Fig. 16. Comparing microstructure evolution of experiment and computational model showing the adiabatic shear band (ASB) and indicating heterogeneous deformation

Particularly at a strain rate of 3500 s^{-1} as shown in Fig. 16, there was a relatively small difference in the plastic deformation across concentric deformation bands. Approximately three concentric deformation bands

were observed with the lowest deformation band occurring at the middle of the specimen and the largest deformation occurring at the outer edges to the cross-sectional area of the impacted plane. The implication of this was that the middle deformation band experienced a contraction at the inner interface and a tension at the outer interface. This resulted in higher shear at the middle deformation band. This could be a possible cause of the ASB reported by Olasumboye et al. [7], Dodd and Bai [19] and Wright [20]. Revealing information such as this could be vital to the computational model.

Also as observed from the PEEQ. Contour plot of the other strain rates, it could be easily seen that similar deformation bands existed but these deformation bands became more pronounced with an increase in strain rate. It was also important to note that from the PEEQ. Contour plots of the other strain rates, the ASB may not always be concentric at all strain rates. This claim was verified in an experimental work done by Owolabi et al. [18] on AA2219-T8 which is also part of the AA 2000 series and had undergone similar heat treatment. Owolabi et al. [18] showed that the adiabatic shear band was circular in a typical cylindrical specimen but may not be perfectly concentric which was similar to the results obtained at other strain rates in the computational model.

Furthermore, a change in temperature of about 101.17^{o}C was observed at a strain rate of 3500 s^{-1}. Including an average ambient temperature of 37^{o}C, the material temperature after impact was estimated to be 138.17^{o}C. This temperature was small compared to the melting point of a typical aluminium allow (527 - 620^{o}C). However, the possibility of temperature change was responsible for the thermal softening and the dissolving of the soluble particles that were reported to be present in the microstructure.

IV. CONCLUSION

The computational model developed for simulating the SHPB setup using AA 2519-T8 demonstrated high accuracy compared to experimental data, with peak stress values deviating by less than 5%. The true stress-true strain curves indicated that the material's response to dynamic loading is strain rate-dependent. The yield point approximated the quasi-static condition, aligning with experimental observations. The extent of deformation varied with strain rates, showing an initial strain hardening followed by perfect plastic flow. Despite discrepancies in true strain values, the overall trends were consistent with experimental results. Applying correction factors to the computational model's true strain values improved the accuracy, suggesting that a generalized correction factor can make computational predictions more reliable. The study highlighted the potential of computational models to serve as a cost-effective and accessible alternative to experimental SHPB setups, making high-strain-rate material testing more feasible for broader engineering applications.

REFERENCES

[1]. Fisher, J., & James, J. (2002). Aluminum alloy 2519 in military vehicles. Materials Science Forum, 160, 43–46.
[2]. Sokkalingam R., Venkatesan K., Sabari S.S., Malarvizhi S., & Balasu bramanian V. (2014). Effect of post-weld aging treatment on tensile properties of gtaw welded armor grade AA2519-T87 aluminum alloy joints. Int. J. Res. Sci. Eng., 3(11), 316–320.
[3]. Xiao X., Zhang W., Wei G., Mu Z., & Guo Z. (2011), Experimental and numerical investigation on the deformation and failure behavior in the Taylor test. Materials & Design 32(5), 2663-2674.
[4]. Lu G., Shen J., Hou W., Ruan D., & Ong L.S. (2008), Dynamic indentation and penetration of aluminium foams, Int. J. Mech. Sci., 50, 932–943.
[5]. [Xie, B., Chen, D., Ding, H., Wang, G., & Yan, Z. (2020). Numerical simulation of Split-Hopkinson Pressure Bar tests for the combined coal-rock by using the Holmquist–Johnson–Cook model and case analysis of outburst. Advances in Civil Engineering, 2020, 1–14.
[6]. Sulaiman, S., Nemati, J., Majzoobi G.H., & AlJermi, M. (2019). Experimental and numerical study of high strain rate property of pure copper processed by ECAE method. Advances in Materials and Processing Technologies 5(3), 386-393.
[7]. Olasumboye A.T., Owolabi G.M., Odeshi A.G., Yilmaz1 N., & Zeytinci A. (2018). Dynamic Behavior of AA2519-T8 Aluminum Alloy Under High Strain Rate Loading in Compression. Journal of Dynamic Behavior of Materials.
[8]. Zhang, W., Tan, P., Liu, W., Zhang, Y., Shi, Z., & Dong, X. (2019). Analytical modeling of a 6061 T8 aluminum alloy-based target impacted by a cone-nose projectile at hypervelocity. International Journal of Impact.
[9]. Afdhal, Annisa. J., Muhammad, A.K., & Leonardo, G. (2016). Development of a Numerical Model for Simulations of Split Hopkinson pressure bar. ARPN Journal of Engineering and Applied Sciences, 11(10), 6657-6662.
[10]. Gupta, M.K. (2021). Numerical simulation of AA7075 under high strain rate with different shape of striker of split Hopkinson Pressure bar. Materials Today Communications 26, 102178.
[11]. Li, Q.M., & Liu, E.L. (2018). Numerical analysis of wetting-induced deformation of rockfill dams. Journal of Engineering Research 5(6), 1-14.
[12]. Li, Y., Jiang, J., Li, W., & Zhu, X. (2020). Dynamic deformation and microstructure evolution of 2024-T351 aluminum alloy using crystal plasticity finite element method. Materials Science and Engineering: A, 791, 139768.
[13]. Mi, B., Zhan, H., & Chen, B. (2020). Numerical simulation of static and dynamic aerodynamics for formation flight with UCAVs. Journal of Engineering Research, 6(3), 203-224.
[14]. Macar M. (2014). Investigation of dynamic behavior of aluminum alloy armor materials. Ph.D. Dissertation, Ankara.
[15]. Thom M. (2017). The elastic-plastic response of aluminum alloys under multiaxial fatigue loading. M.Sc. Thesis, Department of Mechanical Engineering, Howard University, Washington.
[16]. Gray (Rusty) GT III (2000). Classic split-Hopkinson pressure bar testing. In: Kuhn H, Medlin D (eds) ASM handbook, vol. 8. ASM International, Materials Park, 427–430.
[17]. Dassault Systemes (2020). Getting Started with Abaqus: Interactive Edition, 2020. RI, USA: Simulia Corporation, Providence.

[18]. Owolabi G.M., Bolling D.T., Tiamiyu A.A., Abu R., Odeshi A.G., & Whitworth H.A. (2016). Shear strain localization in AA 2219-T8 aluminum alloy at high strain rates. Elsevier: Materials Science & Engineering A, 655 2016, 212–220.
[19]. Dodd, B., & Bai, Y. (2012). Introduction to adiabatic shear localization. In: Adiabatic shear localization. Elsevier, Waltham, 1–20.
[20]. Wright T.W. (2012). Theory of adiabatic shear bands. In: Adiabatic shear localization, 2nd edn. Elsevier, Oxford, pp 215–246.